nature geoscience

SUPPLEMENTARY INFORMATION

DOI: 10.1038/NGEO1949

# Hidden hotspot track beneath the eastern United States

**Risheng Chu[1, 3], Wei Leng[2, 3], Don V. Helmberger[3], and Michael Gurnis[3]**

[1] State Key Laboratory of Geodesy and Earth's Dynamics, Institute of Geodesy and Geophysics, Chinese Academy of Sciences, Wuhan, Hubei 430077, China

[2] Laboratory of Seismology and Physics of Earth's Interior, University of Science and Technology of China, Hefei, Anhui 230026, China

[3] Seismological Laboratory, California Institute of Technology, Pasadena, CA 91125, USA

## Waveform Modeling

Before we can model the *P* waveform data of the Virginia earthquake, we need to determine the source parameters. Our preferred method is the Cut-And-Paste (CAP) method[1], which allows the source parameters to be estimated in the presence of crustal complexity. This technique fits $P_{nl}$ and surface wave segments between observed and synthetics that are allowed to shift independently in timing for alignment (Fig. S1). The earthquake is assumed to be a shear-dislocation with three parameters; strike, dip, and rake. We search for the best-fitting set of parameters as a function of earthquake depth through a grid-search approach[1] (Fig. S1b). During this search, each segment of waveforms is allowed to shift some time to compensate their travel-time residuals generated by heterogeneities in regional crustal structures. The amplitudes are on the same scale except that $P_{nl}$'s are amplified by a factor of 2. Station names and distance are indicated for each station.

Generally, cratons are relatively homogeneous compared to tectonic regions and the shifts are small and the cross-correlation coefficients, numbers below each trace, are high[2]. Note that

synthetics generated from the model in Table S1 fit both the Love waves and $P_{nl}$ waves quite well at these periods. The amplitude of $P_{nl}$ decays with distance $R$ faster than Love waves at a rate of $1/R$ vs. $1/\sqrt{R}$, so that the ratio of $P_{nl}$ and Love amplitudes decreases with distance, for example the two stations MCWV (252 km) and M54A (423 km). The phases $P_n$ and $S_n$ become apparent at the larger distances (arrows). The shape of $P_{nl}$ is mainly controlled by $P_n$, $pP_n$, and $sP_n$. The second pulse about 12 s later is $PP$ or enhanced $P_nP_n$ produced by the gradient in the mantle. Note that $P_n$ is relatively late at station MCWV indicating a reduction of mantle $P$ velocity by over 8%, which will be discussed later. The Love wave, controlled mostly by the structure of upper crust, is also slow which suggests that this slow path has both a crustal and mantle anomaly.

Next we construct synthetics for various models assuming the above source parameters. We then follow a forward modeling approach with a trial-and-error procedure in fitting waveform data. The fits are measured by computing the cross-correlations of synthetics compared with data. As in our recent modeling, we also conducted some grid searches to derive the three models[2] (Fig. S2). Along the profile marked in blue in Fig. 1a, the synthetics generated from velocity model CR agree with data reasonably well (Fig. S2b). However, the corridor from Virginia to the west displays both $P_n$ travel-time delays as well as lack of short-period energy. The $P$ waveforms are about 2 times broader than those along the northern profiles (Fig. S2b). This feature is easily seen in azimuthal sections as presented in Fig. S3a. The broadened waveforms are due to delayed $P$ arrivals that travel in the lower lithosphere between 120 km and 200 km, while $P_n$ arrivals are delayed less. We then adjust velocities in the lower lithosphere to obtain the best fitting 1D model through grid search which are displayed in Fig. S2c. A

transitional profile between CR and the slow corridor has seismic velocities in the lower lithosphere slightly reduced (Fig. S2d).

The azimuthal record sections in Fig. S3a clearly display longer waveform shape along the EW profile near 280°. These elongated signals can be analyzed directly with the application of a multipath detector[3]. The methodology is outlined in Fig. S3b, where in (a) we display $P_n$ (L) and $P$ (R) separately with a timing shift of $\Delta_{LR}$. When summed they produce the lower plot, and next the simulation is compared with the data and aligned to produce $\Delta_T$. Some examples of this simulation are given in (b). The $\Delta_{LR}$ and $\Delta_T$ results are displayed in (c) and (d), respectively, which clearly delineate an EW low-velocity anomaly.

The short-period amplitudes along the slow corridor are quite low (Fig. S4), which can be roughly simulated by applying an attenuation operator t* (ref. 4). We first obtained the source time function by deconvolving theoretical Green's functions from teleseismic waveforms along the west coast using the method described in ref. 5. In order to obtain high-frequency signals attenuated by the mantle, we manually added two spikes to the waveform (inset in Fig. S4). We then calculate synthetics at regional distances using a uniform Q of 1300 and apply an attenuation operator t* to each synthetics to match the observed amplitudes. Since all stations are at similar distances, we can obtain the relative attenuation effect for each path. We have not attempted to match the observed short period signals since they are probably very 3D in nature. Along the profile to the north, which is similar to CR, the t* is close to 0 s indicating very little attenuation. Our slow corridor, however, has significantly large t* values, which are equivalent to Q~180 (shaded area in Fig. S4). Thus, this conduit is heavily attenuated which would be expected if it is associated with mantle upwelling (high temperature). We calculated synthetics

along the slow corridor using Q=180 in the lower lithosphere, and 1300 for everywhere else. The synthetics fit the observed waveforms and amplitudes (Fig. S5).

**Geodynamic Model**

We use a modified version of the 2-D Citcom software with an axisymmetric geometry, mantle compressibility, and adiabatic and viscous heating (the governing equation and model details can be found in ref. 6). The model parameters used are listed in Table S2. We have 257×257 numerical grids for the model domain of 1435 km in radial distance by 2870 km in depth. All the boundaries are free-slip. The top and bottom boundaries are isothermal, and the left and right boundaries are thermally isolated. From the surface to the core-mantle boundary (CMB), the thermal expansivity decreases by a factor of 5, while the thermal diffusivity increases by a factor of 2. We use the Adams-Williamson equation of state[7] which leads to a density increase by a factor of 1.65 from the surface to the CMB. The initial background temperature field consists of an adiabatic profile (computed as in ref. 6) and top and bottom thermal boundary layers of both 100 km in thickness. In the thermal boundary layers, temperature is linearly distributed with depth. The initial compositional field consists of a lithosphere from 0 to 200 km depth (composition $C$ = 1) and a mantle from 200 to 2870 km depth (composition $C$ = 0). Nominally, there is an intrinsic compositional density difference for the lithosphere, 1% lighter than the mantle. We use a viscosity $\eta$ that is temperature-, composition- and depth-dependent:

$$\eta(T,z) = \eta_r(z)\exp[-E_a(T - T_{adi}(z)) + E_c C], \qquad \text{(E1)}$$

where $T$ and z are temperature and depth. $\eta_r(z)$ is the depth-dependent viscosity profile; it is equal to reference viscosity $\eta_0$ in the deep mantle (410 to 2870 km depth), and $\eta_0/100$ in the

shallow mantle (0 to 410 km depth). $T_{adi}$(z) is the initial adiabatic temperature profile. The activation energy $E_a$ determines the viscosity contrast caused by temperature variation. We choose an $E_a$ which leads to a viscosity contrast of $10^{10}$, when the adiabatic temperature profile $T_{adi}$(z) is not considered, for temperature variation between the surface and the CMB. Since we remove $T_{adi}$(z) from the temperature field, the actual viscosity contrast induced by temperature in our model is approximately $10^8$. Nominally, the compositional viscosity parameter $E_c$ is chosen to give a viscosity increase of a factor of 5 for the lithosphere composition.

A plume is induced by slightly perturbing the bottom thermal boundary layer at the center of the domain (setting the temperature to be the CMB temperature in a 100 km by 100 km box at the bottom center). To quantify the plume radius at each depth, the plume region is defined as the area where the temperature $T$ is larger than a threshold:

$$T > T_{ave} + f(T_c - T_{ave}), \qquad \text{(E2)}$$

where $T_{ave}$ and $T_c$ are the horizontally averaged temperature and centerline temperature, respectively; $f$ is a constant. We choose $f = 0.2$ for defining a plume because it can preserve most of the plume heat flux while excluding a large region with positive temperature anomaly but small upward velocities[8].

We are interested in the interactions between the plume conduit (tail) and the lithosphere. After the plume head reaches the bottom of the lithosphere and fully expands horizontally (Fig. S6a), we keep the plume tail beneath 300 km depth (marked by white lines in Fig. S6a) and replace the rest area with the horizontally averaged temperature at each depth. After 3 million years (Myrs), the plume tail reaches the bottom of the lithosphere, spreads out horizontally (Fig. S6c), and slightly erodes the lithosphere at the model center (Fig. S6d). We then artificially

remove the supplying plume conduit by replacing the temperature fields beneath 250 km depth with the horizontally averaged temperature at each depth.

The ponded plume material rises slowly, pushes the lithosphere material aside and forms a concave eroded region at the bottom of the lithosphere. During this erosion process, the temperature anomaly of the plume material decays with time due to thermal diffusion (Fig. S7). We consider the ponded plume material forms a low Q region due to its high temperature. If Q is estimated to be ~180 in this seismically low-velocity corridor, the *P*-wave anomaly due to the temperature variation can be computed from $\partial \ln V_p / \partial T = -1.08$ (ref. 9). For region with higher Q, we use $\partial \ln V_p / \partial T = -0.62$ to compute the temperature induced *P*-wave anomaly[9]. After evolving for 49 and 74 Myrs, the *P*-wave anomaly at the center of the eroded region is about -2.4% and -2.1%, respectively (Fig. 2). Such ponded plume material causes ~15% heat flux anomaly and ~400 m dynamic topography at the surface (Fig. S8). Therefore the surface expression of ponded plume material is relatively weak. However, if the influence of local tectonic setting can be excluded, such a heat flux and dynamic topographic signal caused by the hidden hotspot track may be detectable.

The extent of lithosphere erosion by ponded plume material decreases with increased viscosity contrast $\delta\eta$ and density contrast $\delta\rho$ between the lithosphere and the mantle, so are the size and magnitude of the *P*-wave anomaly region (Fig. S9). If $\delta\rho$ is reduced to 0, e.g. as for oceanic lithosphere, strong lithosphere deformation occurs because the lithosphere cannot self-adjust its depth after temperature anomaly diffuses (Fig. S9d). The extent of lithosphere erosion and the magnitude of the *P*-wave anomaly also increase with Rayleigh number (Fig. S10), suggesting that larger plume flux causes stronger *P*-wave anomalies.

Our nominal computations do not have an imposed plate velocity at the top boundary. Based

on results from 3-D models with imposed plate velocities (e.g. refs. 10, 11, 12), the plume material is carried along (dragged) with the lithosphere after plume impacts the lithosphere. Therefore, there is little relative motion between the lithosphere and the ponded plume material, consistent with our model. Some studies (ref. 13) suggested that an imposed plate velocity might reduce the efficiency of lithosphere erosion by plumes. To test the effects of an imposed plate velocity on our results determined from our nominal computational domain, we employ a 3-D model domain with a plate velocity at the surface using the finite element code CitcomCU[14].

The model geometry is 400 km deep, 1600 km wide and 3200 km long in the direction of plate motion (Fig. S11a). The numerical resolution is 6.25 and 12.5 km in the vertical and the horizontal direction, respectively. The plate velocity is imposed as 2 cm/year along the X direction at the top surface. For the bottom boundary, we have zero tangential velocities and normal stresses (i.e. $V_x=V_y=S_{zz}=0$), and the latter permit vertical flow through it. The top and bottom boundaries are isothermal with temperature fixed at 0 and 1400 $^{o}$C, respectively, except within a circular region at the bottom boundary that maintains the temperature anomalies of the plume conduit. For the left and right side-walls (i.e. YZ-plane at X=0 and 3200 km), we also apply zero tangential velocities and normal stresses (i.e. $V_y=V_z=S_{xx}=0$), the latter permitting horizontal flow through. The left side-wall has a fixed temperature profile which is derived from a half-space cooling model for a 200 Ma old lithosphere. This temperature profile is also used for the whole box as the initial temperature. The right side-wall has a zero temperature gradient in x-direction. Reflecting boundary conditions are applied to the front and rear side-walls (i.e. XZ-plane at Y=0 and 1600 km).

The circular region in the bottom boundary is centered at 800 km away from the left side-wall along the X-axis and maintains a temperature anomaly as $\Delta T = \Delta T_p \exp(-r^2 / R_p^2)$, where

$\Delta T_p$, r and $R_p$ are the plume excess temperature, the horizontal distance to plume center and the plume radius, respectively. For this computation, we set $\Delta T_p$ = 400 K and $R_p$ = 75 km. Initially, we put a plume conduit extending 200 km above the circular region and having the same temperature anomaly as the region (Fig. S11a). The compositional continental lithosphere extends from surface to 200 km depth. The viscosity structure is the same as we used for the 2-D modeling, except that we now impose a maximum viscosity $\eta_{max}$ = 1.0e23 Pas and a minimum viscosity $\eta_{min}$ = 2.5e18 Pas to avoid numerical difficulties in solving the Stokes equation.

After the model reaches a steady state, the plume material is sheared beneath the moving lithosphere and cools with distance (Fig. S11b). Due to the erosion effect, the compositional continental lithosphere is thinned from the bottom. Such a thinning effect can be transported to several thousand kilometers away due to the plate motion (Fig. S11b). The cross-sections at 50 and 75 Myrs after the plate passes above the plume center correspond to YZ-plane at X=1800 and 2300 km, respectively. The residual temperature, compositional field and induced *P*-wave anomaly on these two cross-sections (Fig. S11c) are very close to our previous 2-D results, supporting the idea that our 2-D model is a good simplification for studying the plume-lithosphere interactions. To test the effects of different plate velocities on our results, we double the plate velocity and the length of the box to 4 cm/year and 6400 km, respectively. The cross-sections at 50 and 75 Myrs, now corresponding to YZ-plane at X=2800 and 3800 km, show that the magnitude of residual temperature, erosion height and induced *P*-wave anomaly become smaller for the increased plate velocity (Fig. S11d). This suggests that the plate velocity does affect the efficiency of lithosphere erosion by plumes (ref. 13).

**References**:

1. Zhu, L. & Helmberger, D. V. Advancement in source estimation techniques using broadband regional seismograms. *Bull. Seismol. Soc. Am.* **86**, 1634-1641 (1996).
2. Chu, R., Schmandt, B. & Helmberger, D. V. Upper mantle *P* velocity structure beneath the Midwestern United States derived from triplicated waveforms. *Geochem. Geophys. Geosyst.* **13**, Q0AK04 (2012).
3. Sun, D., Helmberger, D. V. & Gurnis, M. A narrow, mid-mantle plume below southern Africa. *Geophys. Res. Lett.* **37**, L09302 (2010).
4. Helmberger, D. V. Theory and application of synthetic seismograms, earthquakes: observations, theory and observations, *Proceedings of the International School of Physics*, Enrico Fermi Course LXXXV, H. Kanamori and E. Boschi, Editors, North-Holland, Amsterdam, 174-217 (1983).
5. Chu, R., Zhu, L. & Helmberger, D. V. Determination of earthquake focal depths and source time functions in central Asia using teleseismic *P* waveforms. *Geophys. Res. Lett*. **36**, L17317 (2009).
6. Leng, W. & Zhong, S. J. Surface subsidence by mantle plume and volcanic loading in large igneous provinces. *Earth Planet. Sci. Lett*. **291**, 207-214 (2010).
7. Birch, F. Elasticity and constitution of the Earth's interior. *J. Geophys. Res*. **57**, 227-286 (1952).
8. Leng, W. & Gurnis, M. Shape of thermal plumes in a compressible mantle with depth-dependent viscosity. *Geophys. Res. Lett*. **39**, L05310 (2012).
9. Karato, S.-I. Importance of anelasticity in the interpretation of seismic tomography. *Geophys. Res. Lett*. **20**, 1923-1926 (1993).

10. Ribe, N. M. & Christensen, U. R. Three-dimensional modeling of plume-lithosphere interaction. *J. Geophys. Res*. **99**, 669-682 (1994).
11. Moore, W. B., Schubert, G. & Tackley, P. Three-dimensional simulations of plume-lithosphere interaction at the Hawaiian swell. *Science* **279**, 1008-1011 (1998).
12. Asaadi, N., Ribe, N. M. & Sobouti, F. Inferring nonlinear mantle rheology from the shape of the Hawaiian swell. *Nature* **473**, 501-506 (2011).
13. Manea, V. C., Manea, M., Leeman, W. P. & Schutt, D. L. The influence of plume head-lithosphere interaction on magmatism associated with the Yellowstone hotspot track. *J. Volcanol. Geotherm. Res*. **188**, 68-85 (2009).
14. Zhong, S. J. Dynamics of thermal plumes in 3D isoviscous thermal convection. *Geophys. J. Int*. **162**, 289-300 (2005).
15. Williams, Q. & Revenaugh, J. Ancient subduction, mantle eclogite, and the 300 km seismic discontinuity. *Geology* **33**, 1-4 (2005).
16. Herrmann, R. B. Surface wave focal mechanisms for eastern North American earthquakes with tectonic implications. *J. Geophys. Res*. **84**, 3543–3552 (1979).

**Fig. S1.** Cut-and-Paste (CAP) inversion of the Virginia earthquake determined by modeling regional broadband waveforms, which are arranged according to their azimuths. The $P_n$ waves are filtered using frequencies 5-50 s and surface waves are filtered using frequencies 10-50 s. The best-fitting mechanism is a thrust event at the depth of 6 km. The crust velocity model used here is given in Table S1. (a) Observed velocity data is shown as black traces, and red traces are the corresponding synthetic velocity seismograms. The time shifts relative to the synthetic segments generated from the 1D model are given in c and d, and the cross-correlation coefficient

(CC) in colored triangles at each station. The dashed line denotes the approximate northern limit of the proposed hotspot track. The control on depth is produced by the separation between $P_n$ and the depth phases $pP_n$ and $sP_n$ (ref. 2) (b) The misfit is plotted against depth.

**Fig. S2.** Comparison of three record sections with observations along the northern profile CR (I), Fig. 1; the east-west profile II (a), and a profile in the middle transition (III). The best fitting synthetics for these three models are displayed as overlays in b, c, and d where dotted lines indicate the principle arrivals. The upper 200 km of these models is used to construct the conduit shape displayed in Fig. 3. The X denotes the X discontinuity[15].

**Fig. S3a.** Unfiltered vertical displacement recorded by TA of the Virginia earthquake at distances of $9^o$ to $13.5^o$, respectively, as plotted in azimuth. The data is broken into 0.5° intervals and the waveforms are plotted using a reduced velocity of 8.7 km/s. Red crosses denote handpicked arrival times. Numbers above each waveform correspond to the amplitude ratio of short period (0.5-2.0 s) to long period (2.0-100 s). Note the short-period depletion near azimuths of $280^o$.

Fig. S3b. Summary of multipath analyses. The methodology is reviewed in (a) providing $\Delta_{LR}$ and $\Delta_T$. Some examples are given in (b) with large separations at the smaller distances. The fits are measured with the cross-correlation given after the station names. The results are displayed in (c) and (d). Because these delays are accumulative we also have included the values at the midpoints indicated by the small triangles.

**Fig. S4**. Comparison of short period (0.5-2.0 s) data (black) and synthetics (red) generated using different t* and velocity models. The numbers before each trace are the t*, while the bars on the right are velocity models color-coded in Fig. S2a. The shaded area denotes our corridor with

weakened lower lithosphere. The inset shows the source-time function obtained from stations at west coast.

**Fig. S5**. (a) Ray paths at distances between $8^o$ and $18^o$ for velocity model $CR^2$. (b) *P*-wave velocity (red) and Q (black) model along our corridor. Broadband waveform fits of data (black) and synthetics (red) are shown in (c).

**Fig. S6**. (a) The residual temperature (i.e. the temperature after the horizontally averaged temperature is subtracted) after a mantle plume reaches the bottom of the lithosphere and fully expands in the horizontal direction. The white line marks the boundary of the plume tail beneath 300 km depth, detected from a temperature criterion (see SI text). (b) The averaged mantle temperature (red), plume temperature at the centerline (green) and averaged mantle viscosity (blue) versus depth for (a). The plume tail marked by the white line in (a) continues to evolve for 3 Myrs, spreads beneath the lithosphere and slightly erodes the lithosphere at the model center. (c) and (d) show the residual temperature and composition fields of the plume tail at 3 Myrs.

**Fig. S7**. (a), (b) and (c) show a series of snapshots of the residual temperature for the ponded plume material beneath the lithosphere after evolving for 5, 9 and 19 Myrs. (d), (e) and (f) show compositional fields with $C$=1 for lithosphere and $C$=0 for asthenosphere, corresponding to (a), (b) and (c). The white lines show the compositional interface with $C$ = 0.5. It can be observed that the thickness of the lithosphere at the center becomes less with time. The magnitude of temperature anomaly decreases with time.

**Fig. S8**. The dynamic topography (red) and heat flux (blue) at the surface for the ponded plume material after it evolves for 49 (solid) and 74 Myrs (dashed), respectively.

**Fig. S9**. The residual temperature (a-d), corresponding compositional fields (e-h) and *P*-wave anomalies due to temperature increase (i-l) for four cases with different $\delta\rho$ and $\delta\eta$ after ~50 Myrs

of the evolvement of ponded plume material. (a) : $\delta\rho$ = -1.0% and $\delta\eta$ = 10; (b): $\delta\rho$ = -1.0% and $\delta\eta$ = 20; (c): $\delta\rho$ = -2.0% and $\delta\eta$ = 10; (d): $\delta\rho$ = 0.0% and $\delta\eta$ = 10.

**Fig. S10**. The residual temperature (a and b), corresponding compositional fields (c and d) and *P*-wave anomalies due to temperature increase (e and f) for two cases with different Rayleigh number after ~50 Myrs of the evolvement of ponded plume material. (a): $Ra = 1.0\times10^7$; (b): $Ra = 4.0\times10^7$.

**Fig. S11**. (a) The model geometry for our 3-D model with plate motion at the top surface. The plate velocity is 2 cm/year along the X direction. The temperature on the YZ-plane at X=0 shows the imposed temperature boundary condition. The plume conduit is initially centered at 800 km along the X-axis, as shown by the half cylinder colored with temperature. (b) The residual temperature (top) and the compositional field (bottom) on the XZ-plane at Y=0, after the model reaches a steady state. (c) The residual temperature, compositional field and *P*-wave anomalies on the YZ-plane at X=1800 and 2300 km, respectively, corresponding to the time frame of 50 and 75 Myrs after plate passes above the plume center. (d) Similar to (c), except that the plate velocity is doubled to 4 cm/year and the box size in the X direction is doubled to 6400 km. Therefore, YZ-plane at X=2800 and 3800 km now corresponds to the time frame of 50 and 75 Myrs after plate passes above the plume center.

**Fig. S12.** Presentation of data and modeling along the northeast corridor. The travel-time delays relative to CR predictions and the product of $\Delta t$ and long-period/short-period ratio are shown in (a) and (b), respectively. The blue line denotes the proposed hotspot track. The fits of data (black) and synthetics (red) for northeastern stations are shown in (c), filtered to 2-100 s. The velocity model is M2 displayed in Fig. 1. Waveforms between $9^o$ and $12^o$ are enlarged in (d) indicating two arrivals, $P_n$ and $P$ denoted by dotted and solid blue lines, respectively. For

comparison, waveform fits for stations to the north, which are similar to CR, are shown in (e) with a single *P* arrival. The uncertainty is greater than the east-west section in Fig. 1 because of lack of station density. However, the existing data along the corridor clearly displays a delayed *P* onset relative to paths along the northern direction indicative of a low velocity corridor.

**Table. S1.** Velocity model for inversion of the regional focal mechanism[16]

| Thickness (km) | Vs (km/s) | Vp (km/s) |
|---|---|---|
| 1.0 | 2.89 | 5.00 |
| 9.1 | 3.52 | 6.10 |
| 10.0 | 3.70 | 6.40 |
| 20.0 | 3.87 | 6.70 |
| 5.0 | 4.67 | 8.31 |
| 5.0 | 4.67 | 8.33 |
| 5.0 | 4.68 | 8.34 |

**Table. S2** Physical parameters used in the geodynamic modeling[a]

| Parameters | Value |
|---|---|
| Mantle thickness $d$ | 2870 km |
| Surface thermal expansivity $\alpha_0$ | $3.0\times10^{-5}$ /K |
| Surface thermal diffusivity $\kappa_0$ | $1\times10^{-6}$ m$^2$/s |
| reference density $\rho_0$ | 3300 kg/m$^3$ |
| reference specific heat $C_{p\_0}$ | 767 J/(kgK) |
| reference gravitational acceleration $g_0$ | 10.0 m/s$^2$ |
| Mantle compressibility $\chi$ | 0.5 |
| Surface temperature $T_{s\_0}$ | 273 K |
| Temperature contrast between surface and bottom $\Delta T$ | 3500 K |
| Reference viscosity $\eta_0$ | $4.0\times10^{21}$ Pa s |
| Dissipation number $D_i = (\alpha_0\, g_0\, d) / C_{p\_0}$ | 1.12 |
| Rayleigh number $Ra = (\rho_0\, \alpha_0\, g_0 \Delta T\, d^3) / (\kappa_0\, \eta_0)$ | $2.0\times10^7$ |

[a] The thermal expansivity decreases by a factor of 5 from surface to the CMB, while the thermal diffusivity increases by a factor of 2 from surface to the CMB. The density increases by a factor of 1.65 from surface to the CMB. Reference specific heat and gravitational acceleration are constant throughout the mantle.

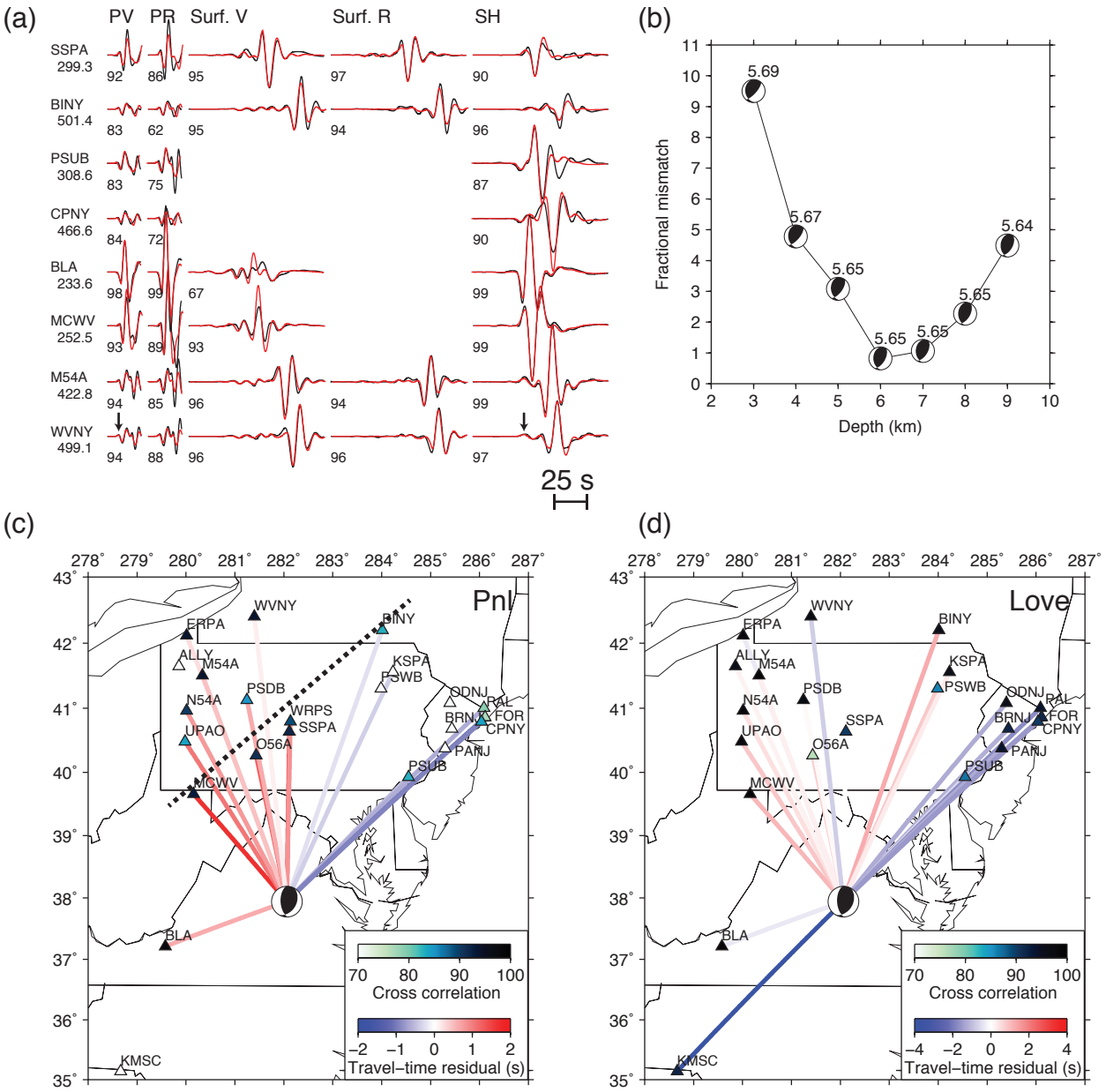


Figure S1

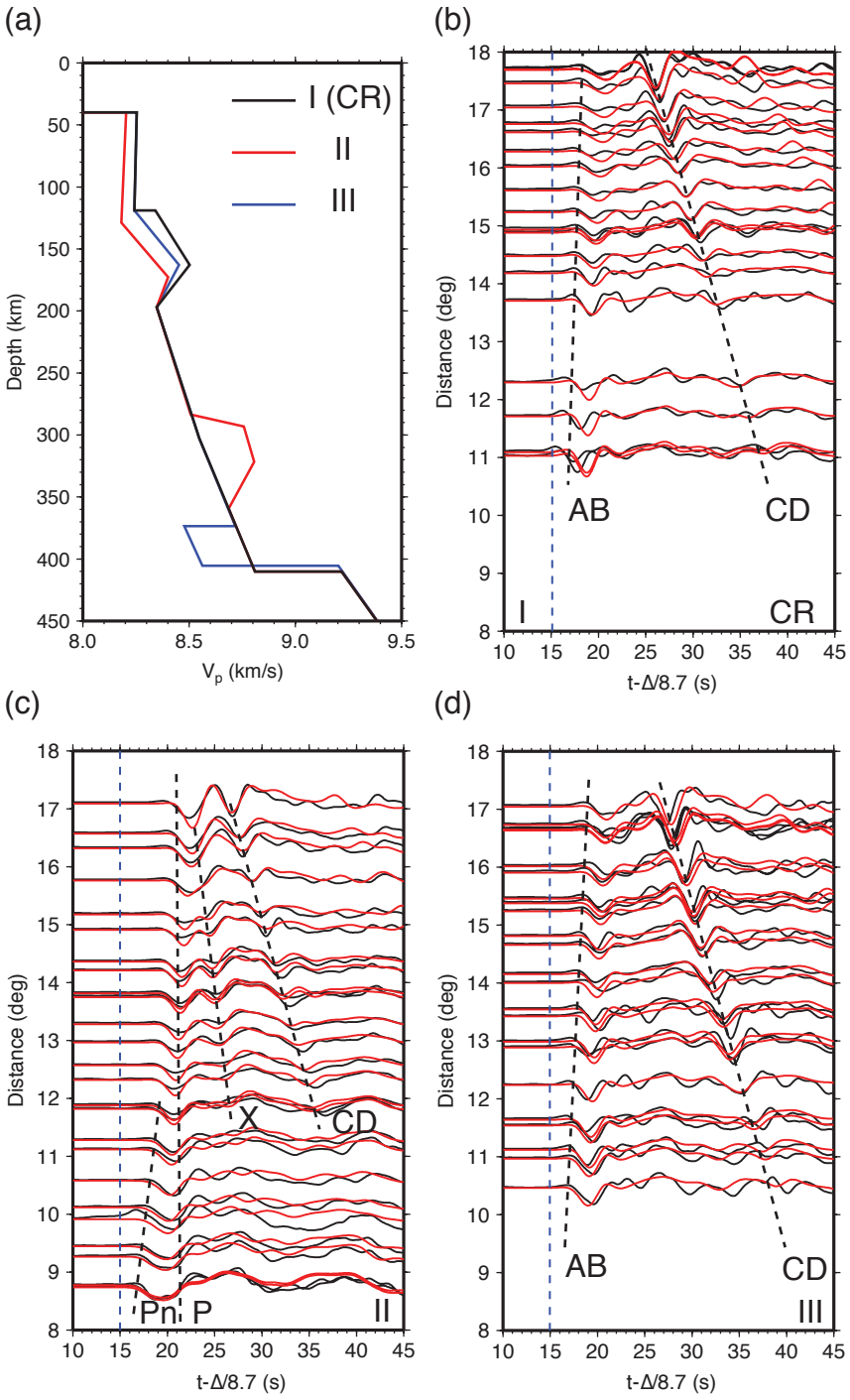


Figure S2

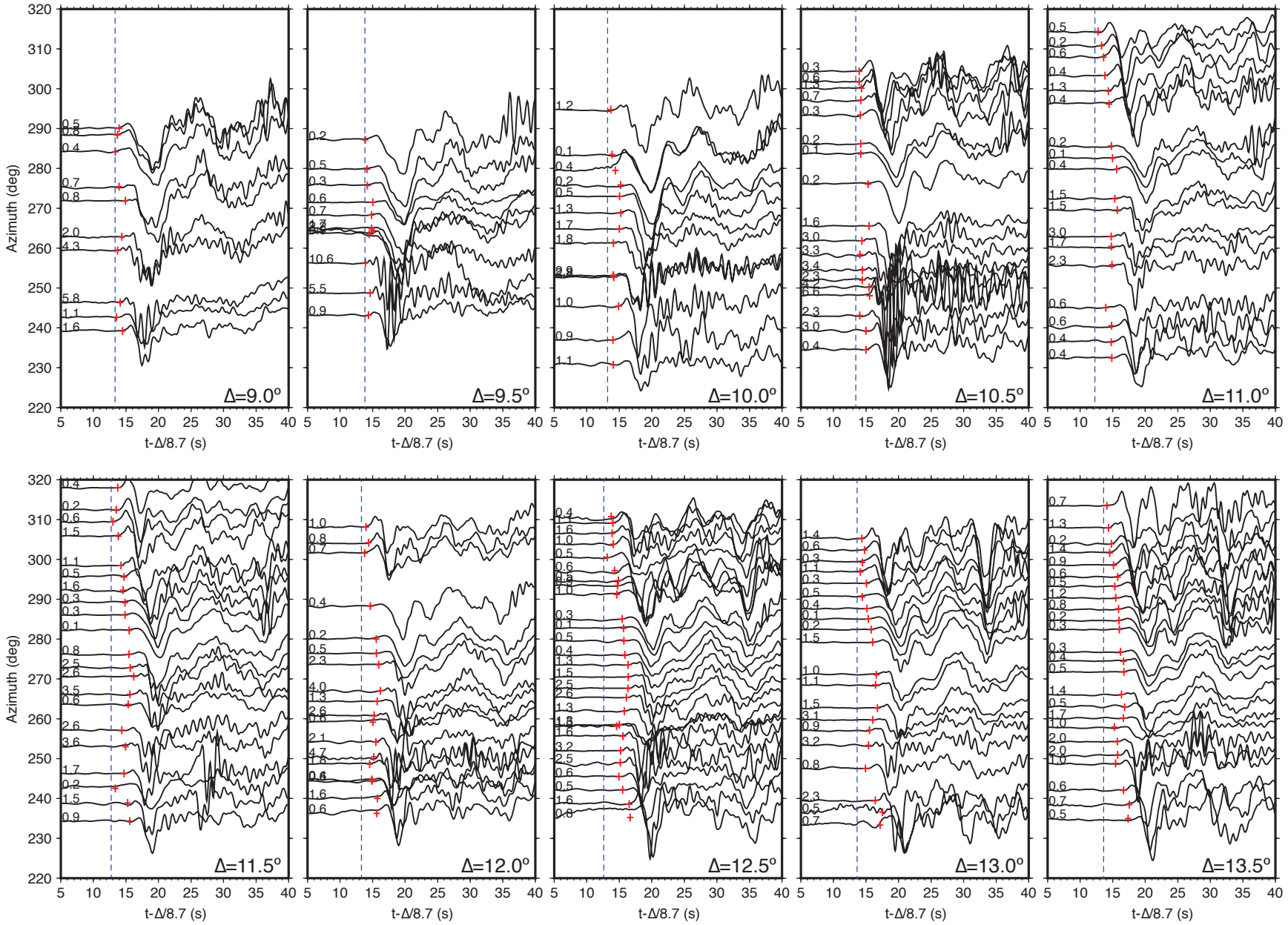


Figure S3a

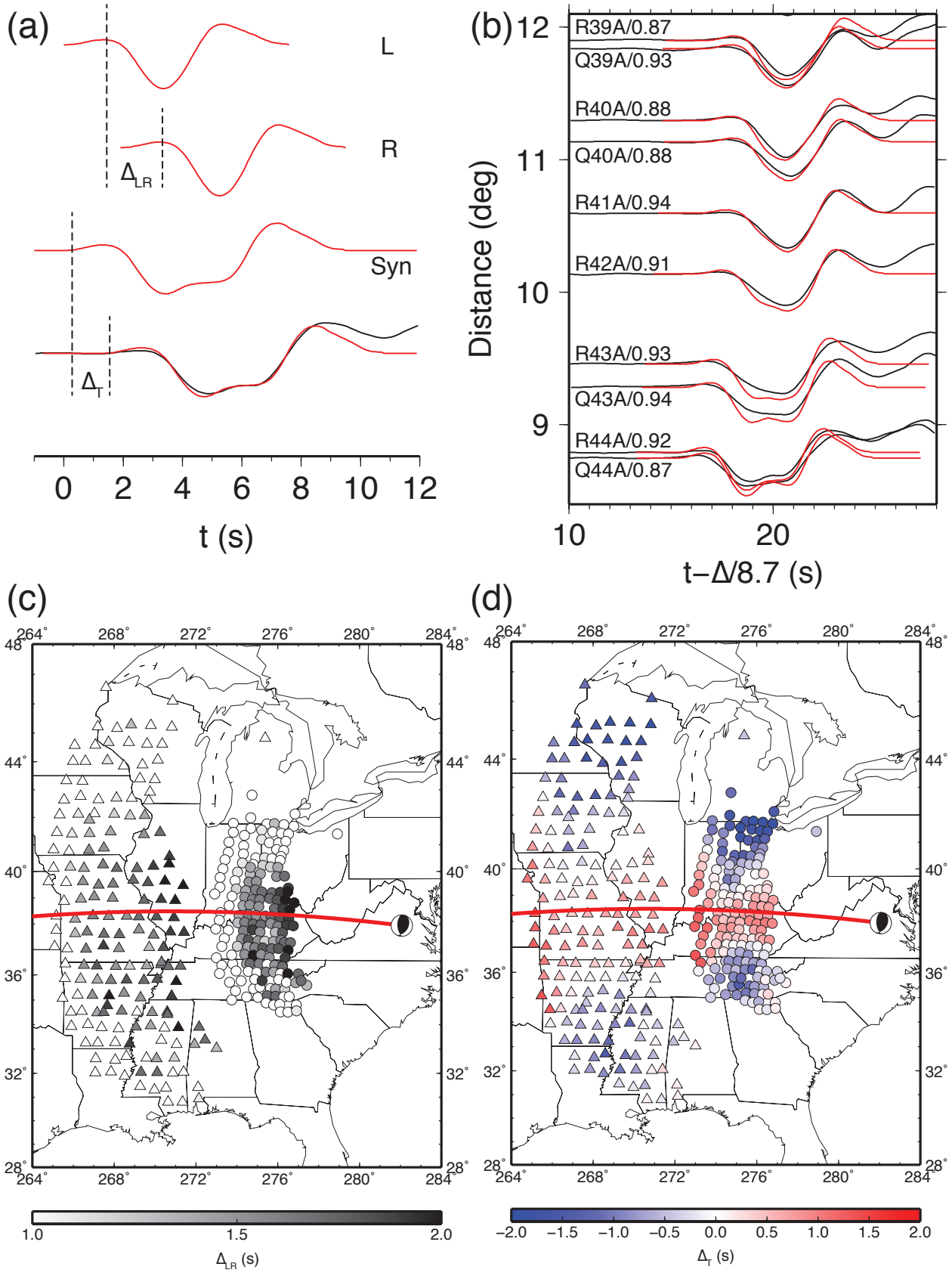


Figure S3b

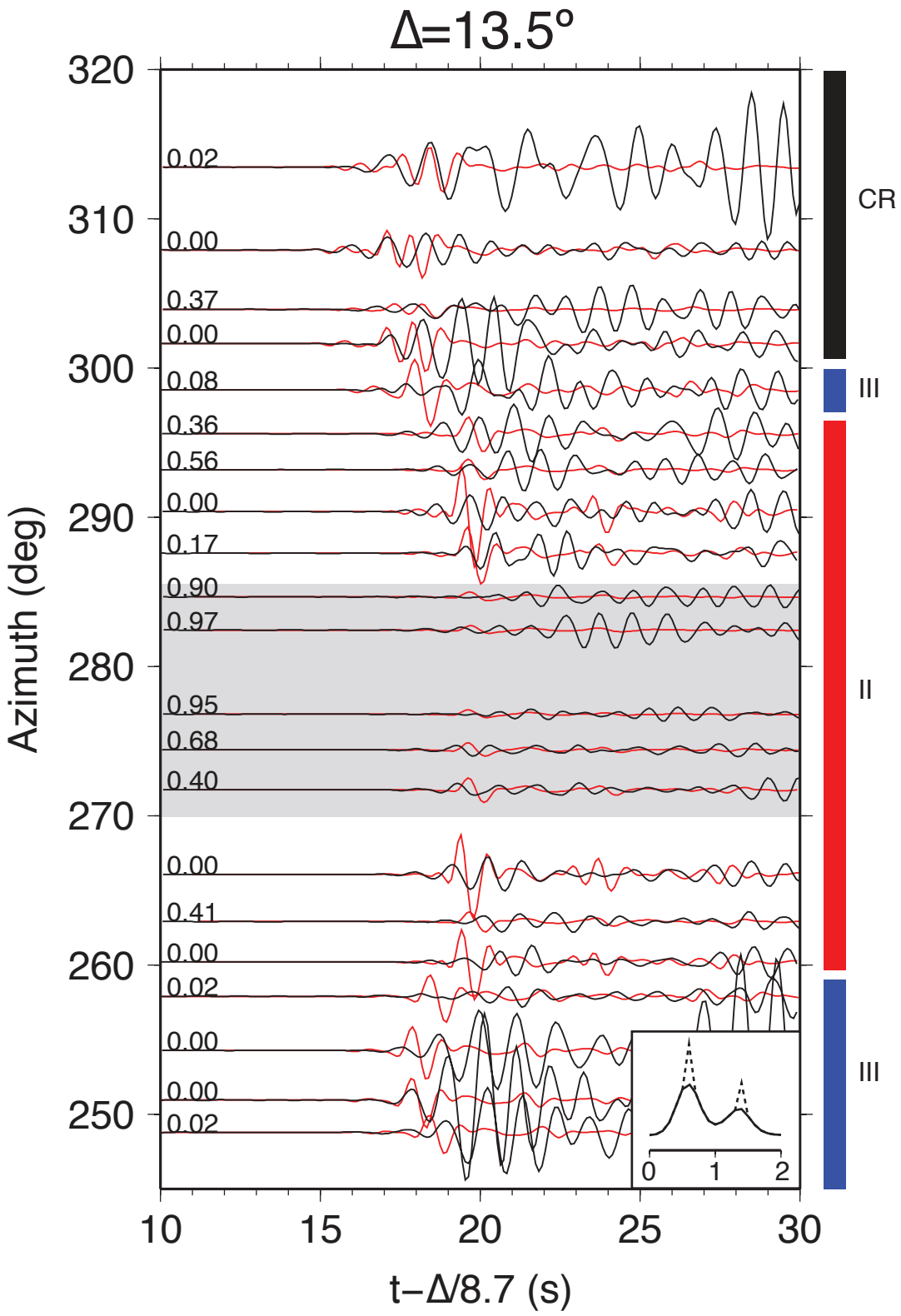


Figure S4

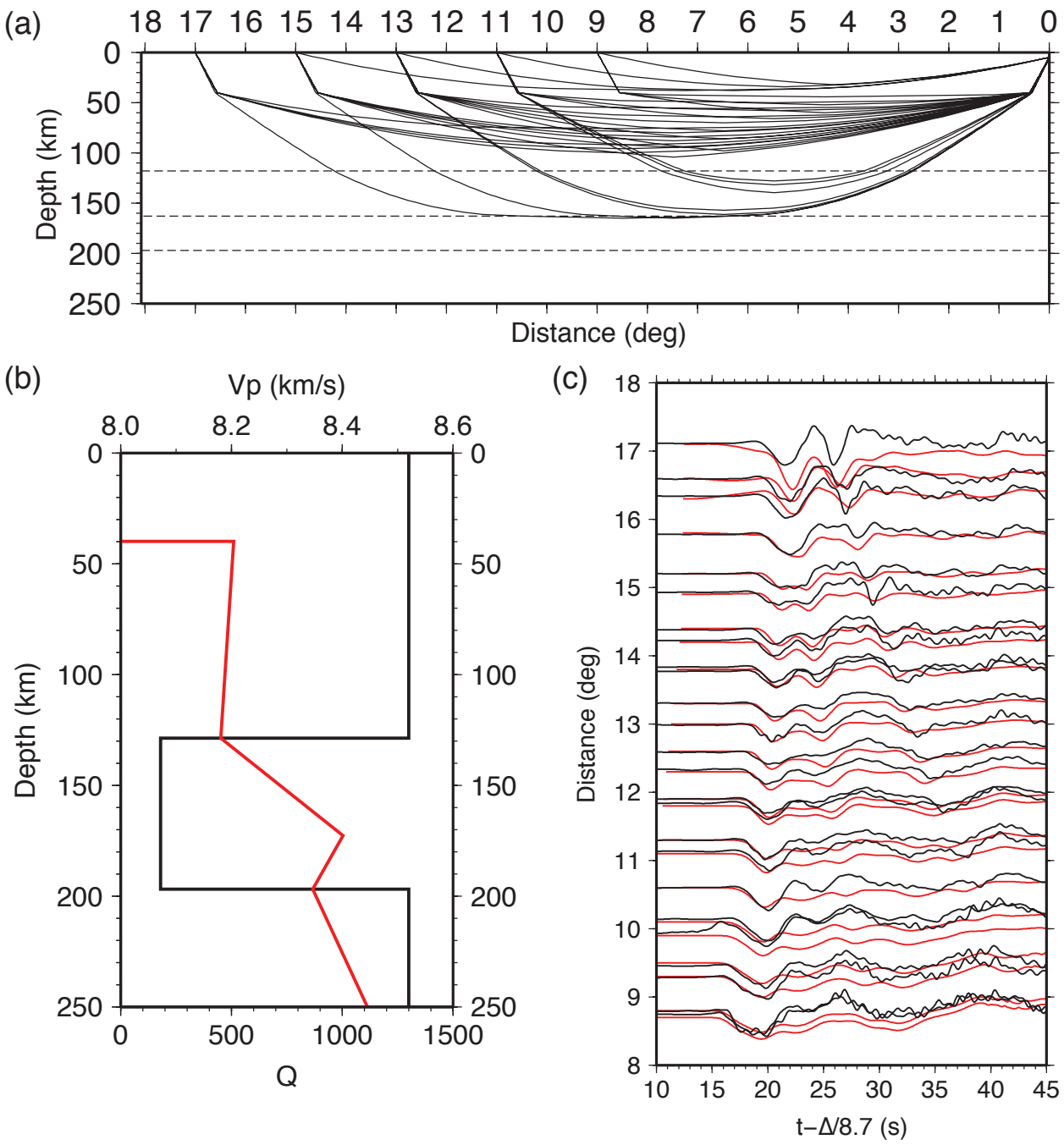


Figure S5

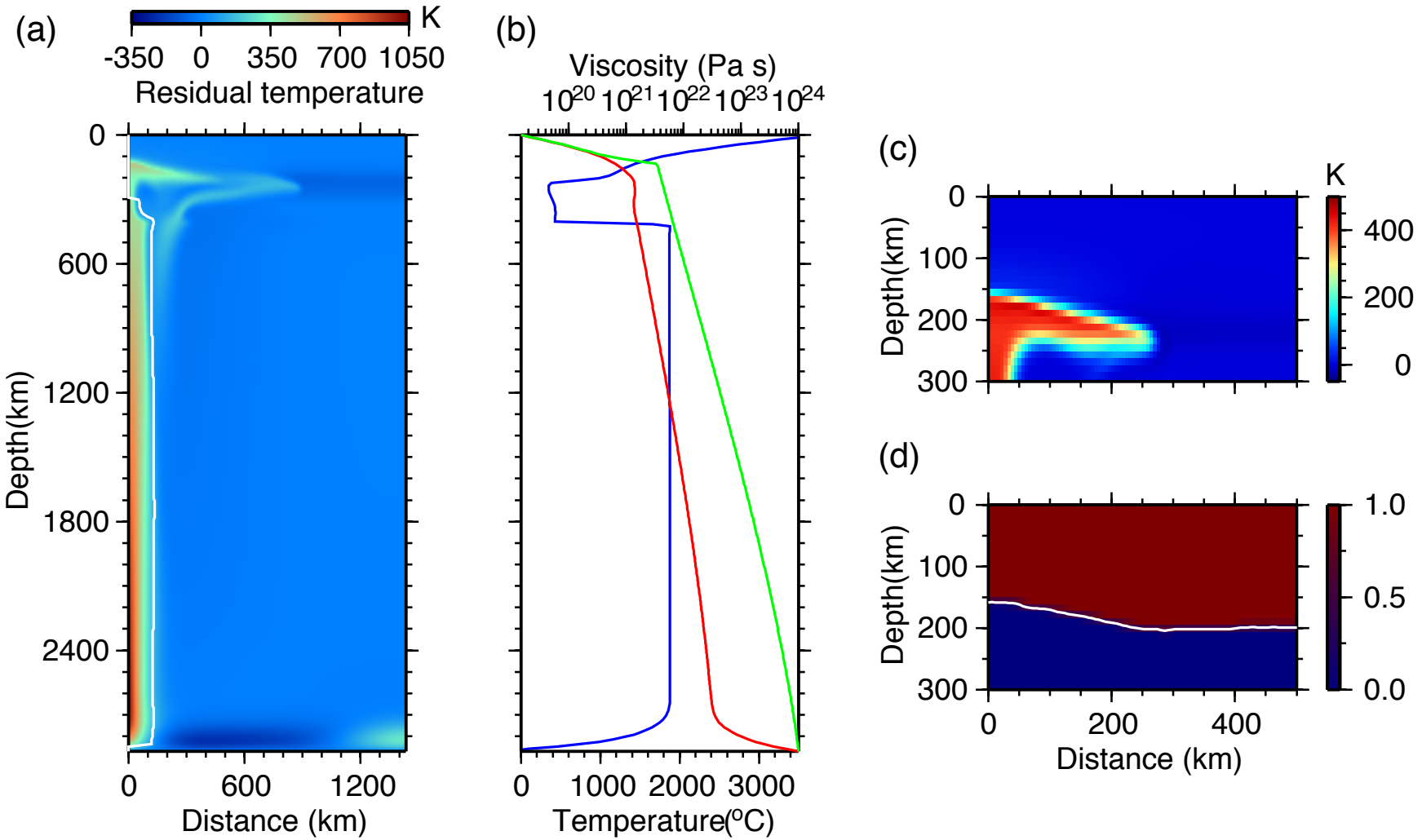


Figure S6

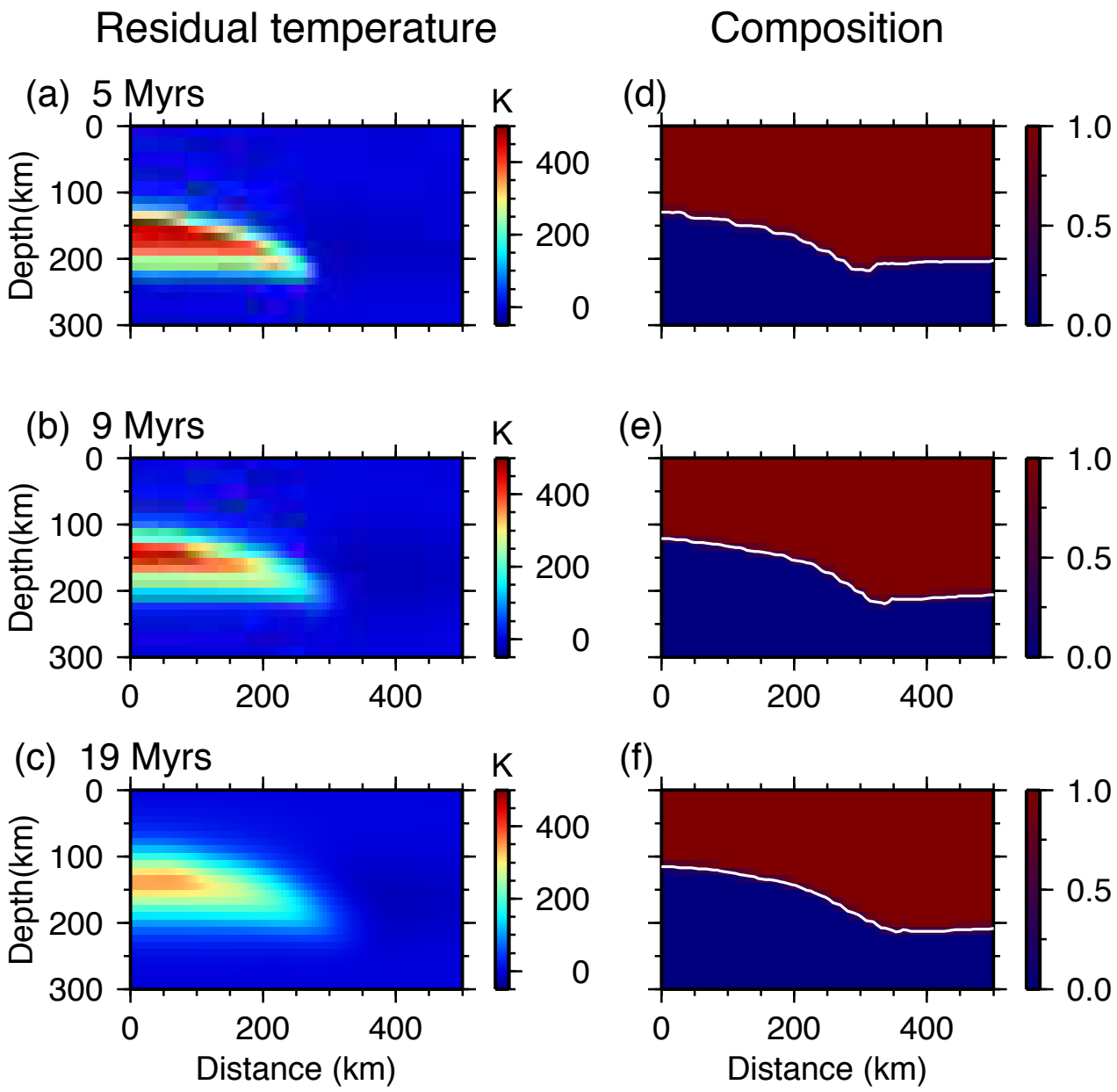


Figure S7

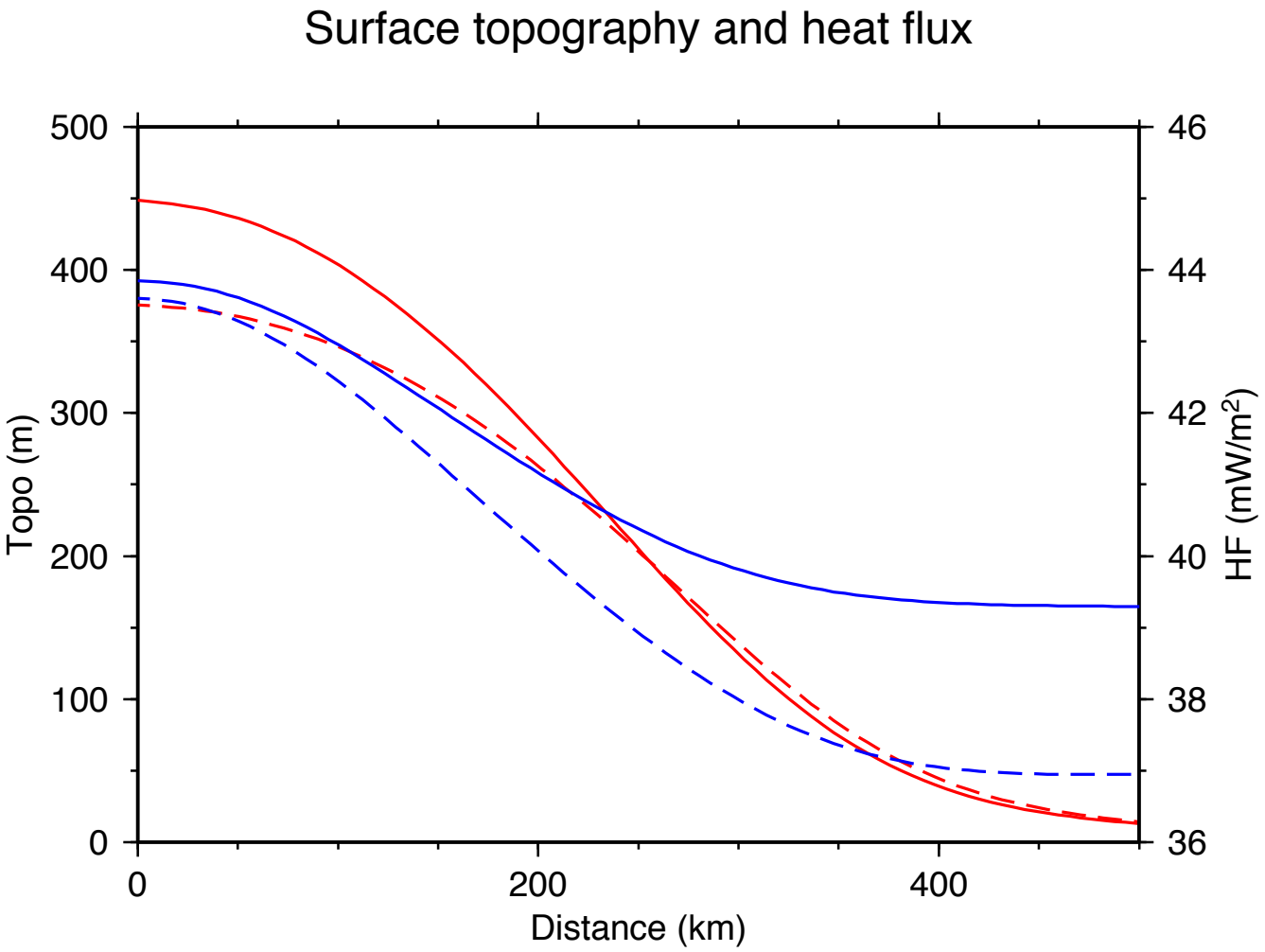


Figure S8

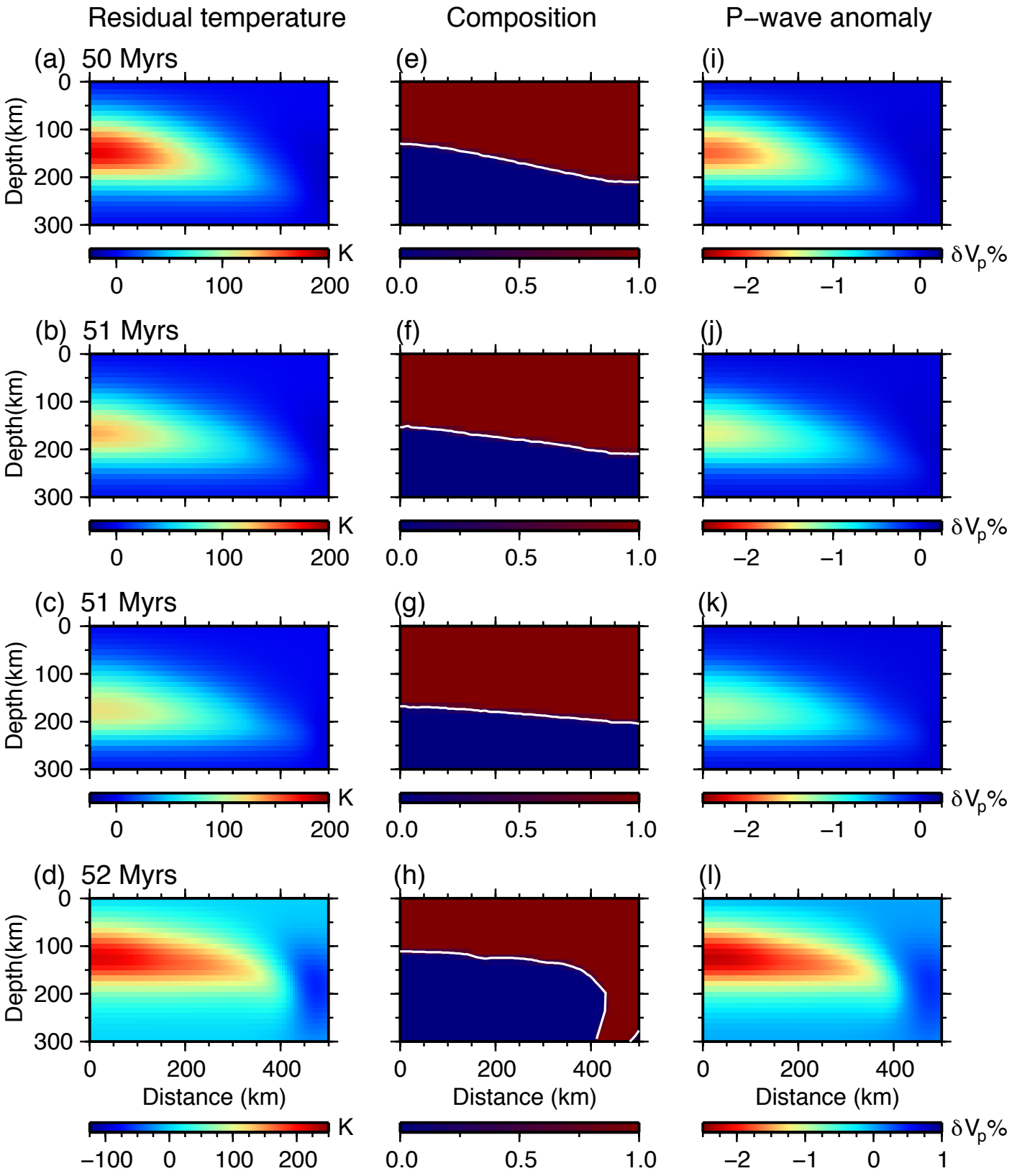


Figure S9

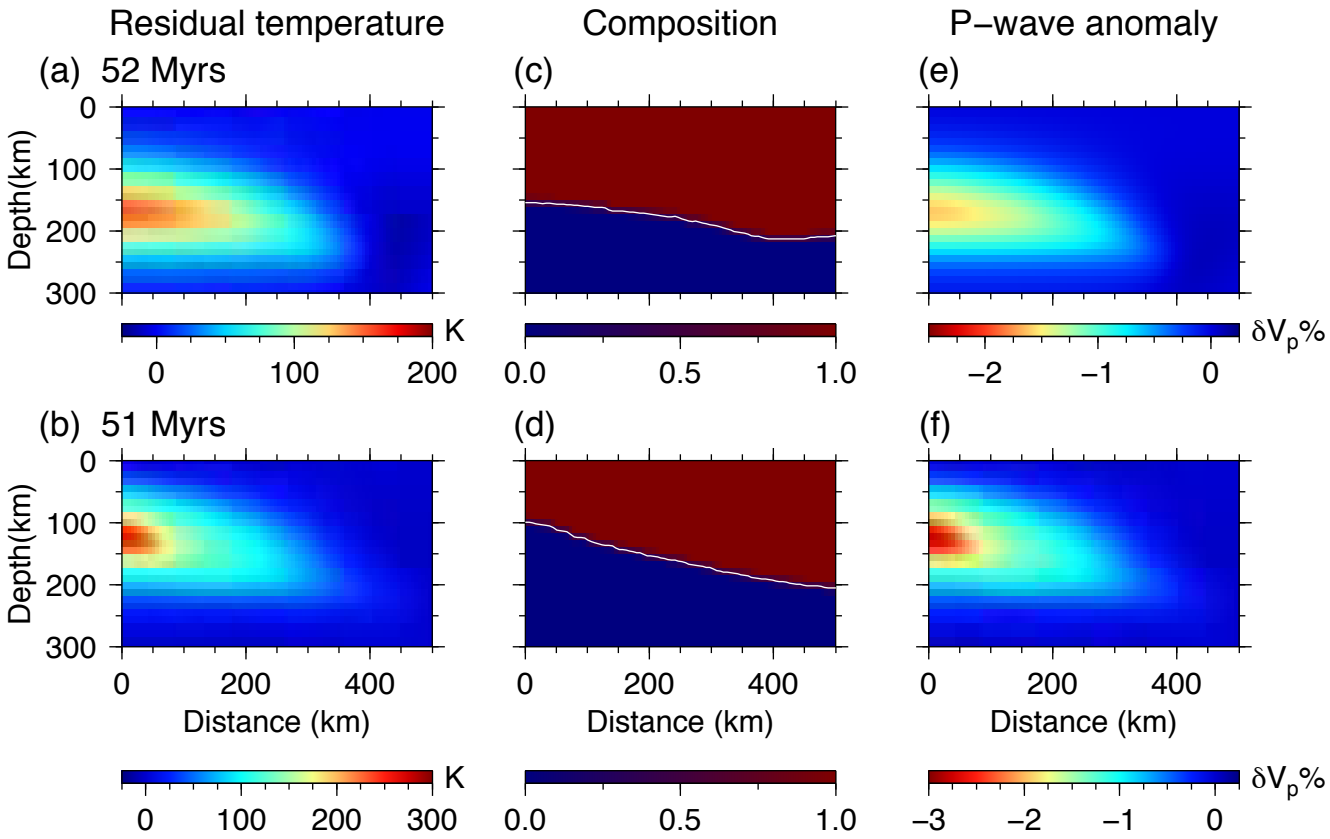


Figure S10

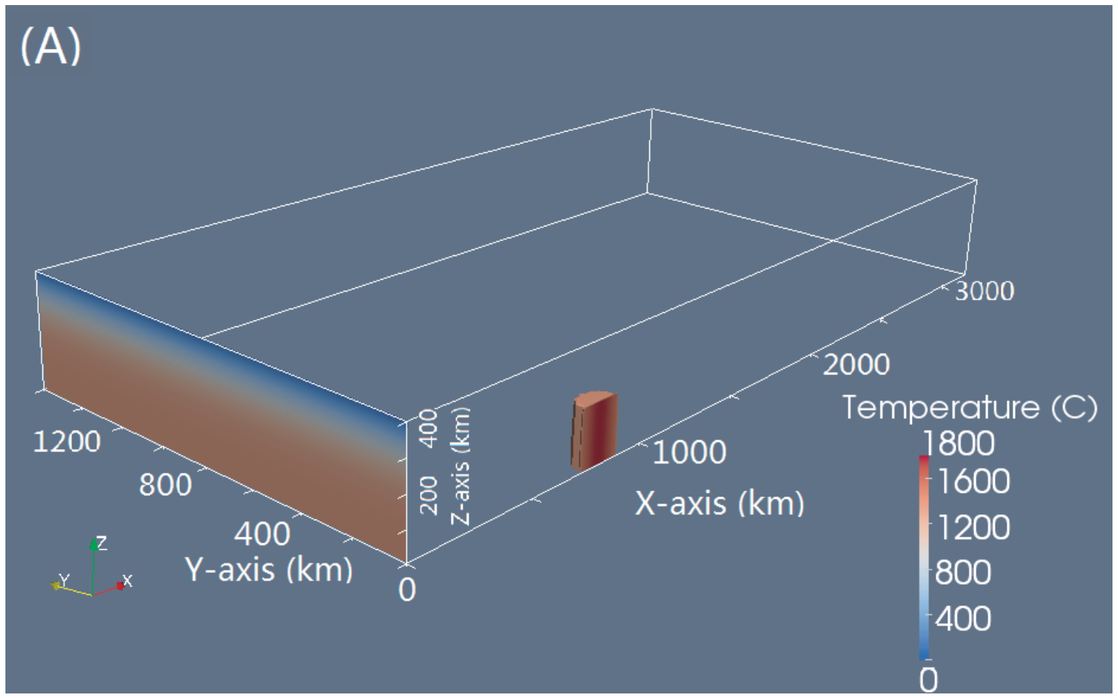


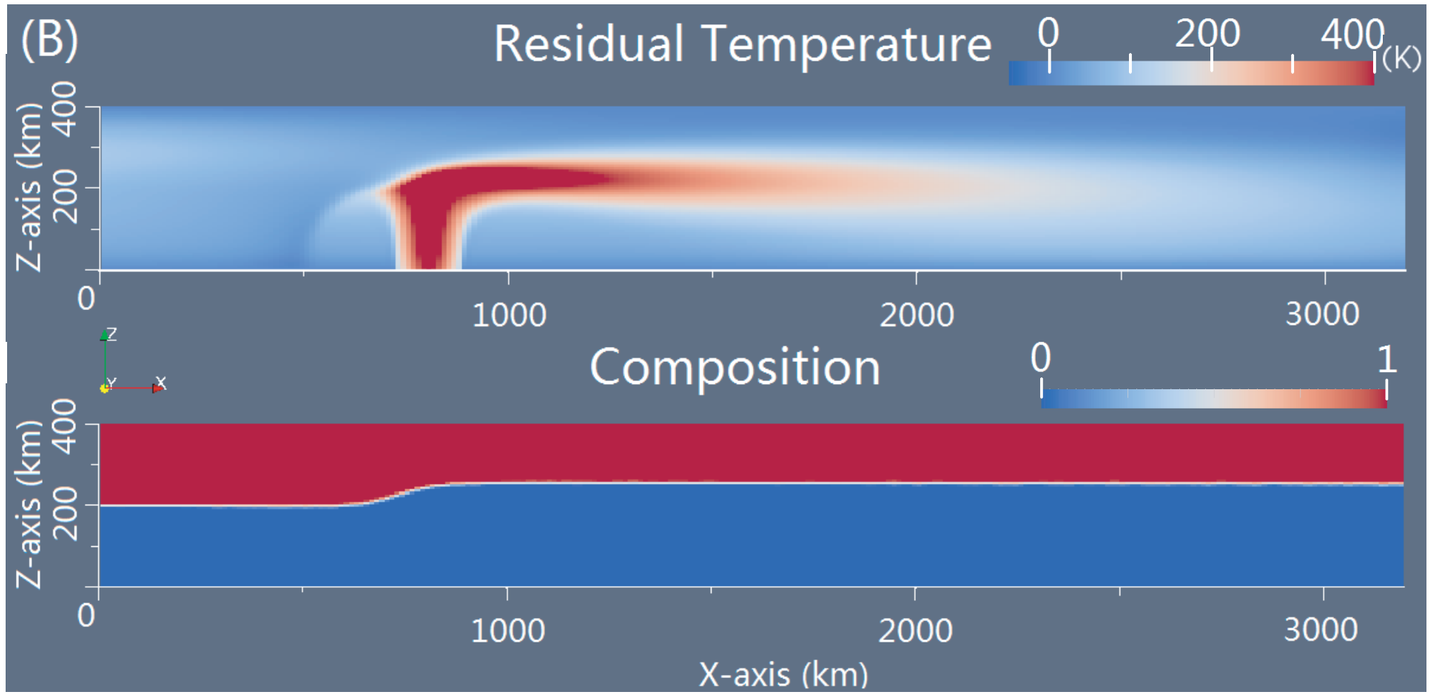


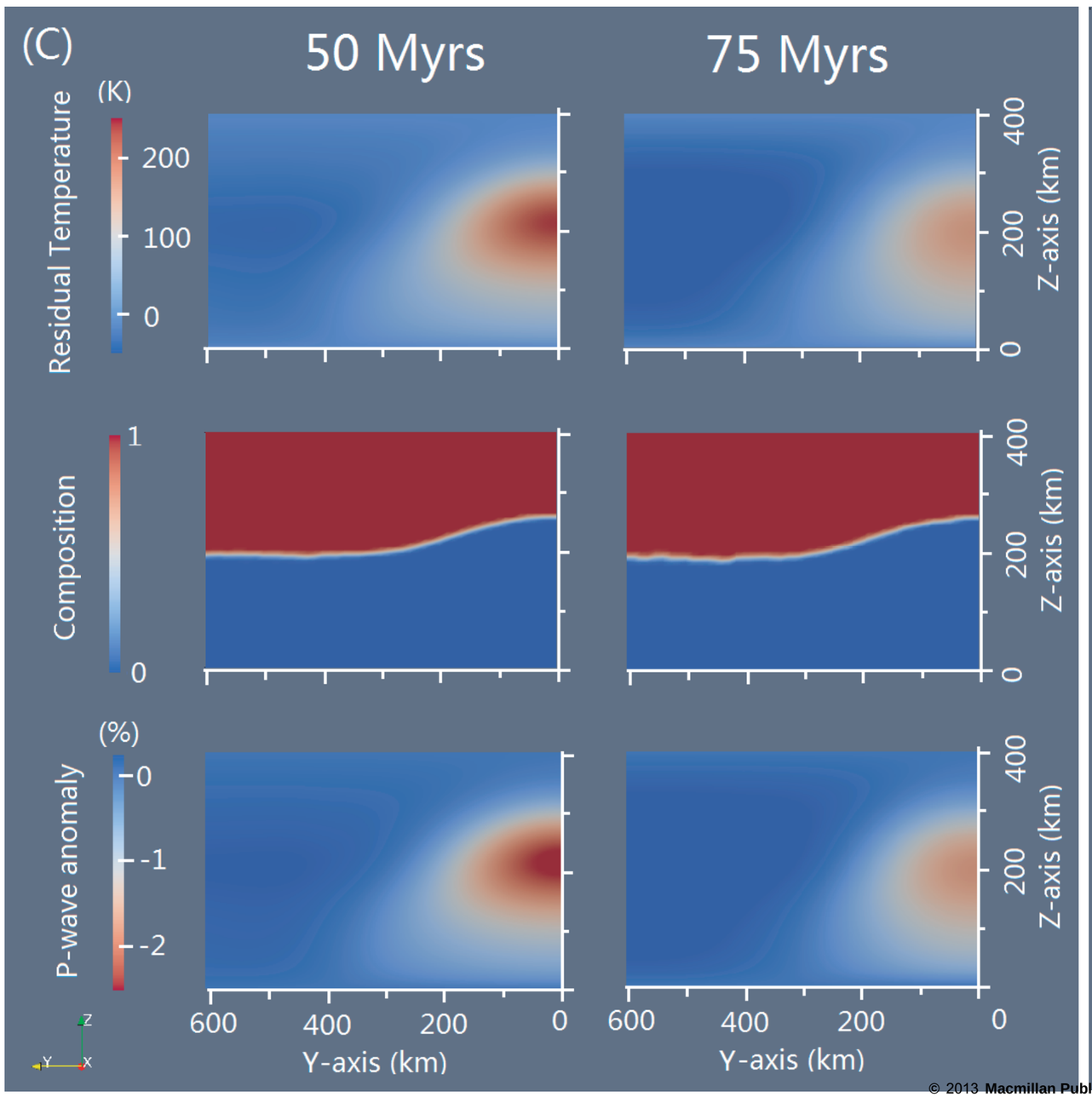


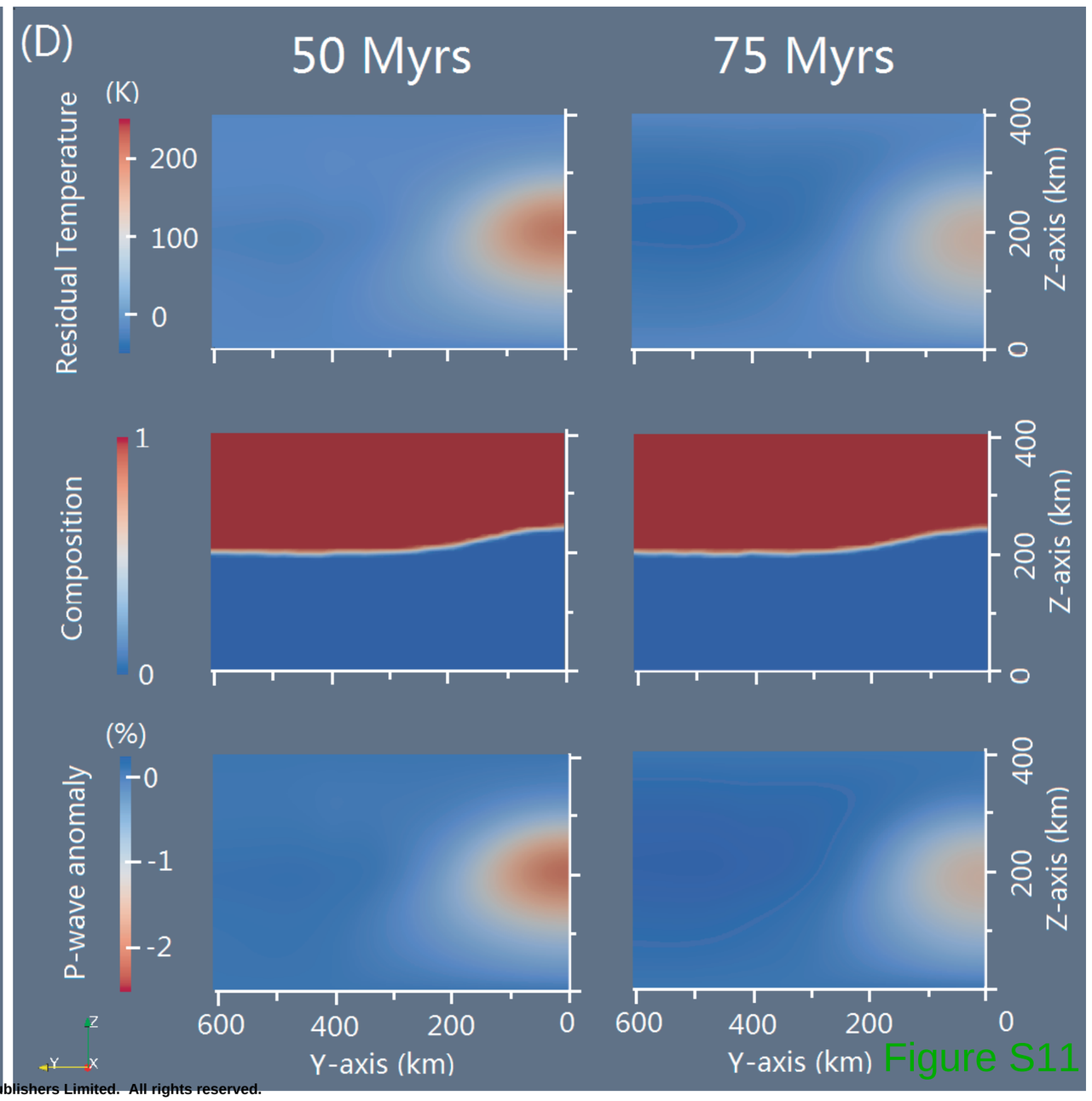


Figure S11

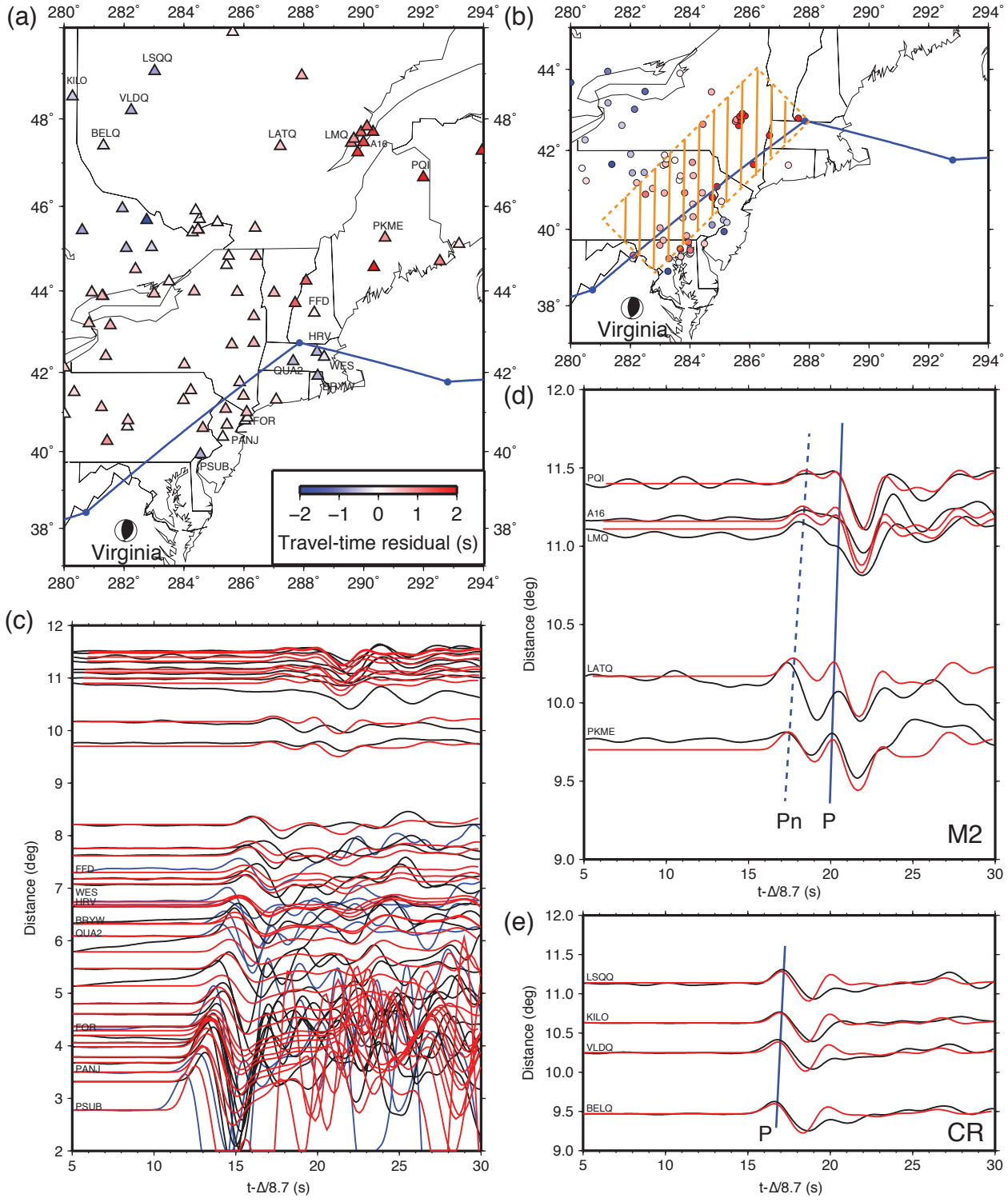


Figure S12